











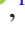




New giant planet beyond the snow line for an extended MOA exoplanet microlens sample

Clément Ranc ^{1,★}, David P. Bennett ^{2,3}, Richard K. Barry ², Naoki Koshimoto ^{4,5}, Jan Skowron ⁶, Yuki Hirao,⁷ Ian A. Bond,⁸ Takahiro Sumi ⁷, Lars Bathe-Peters ^{7,9,10}, Fumio Abe,¹¹ Aparna Bhattacharya,^{2,3} Martin Donachie,¹² Hirosane Fujii,⁷ Akihiko Fukui ^{13,14}, Stela Ishitani Silva ^{2,15}, Yoshitaka Itow ¹¹, Rintaro Kirikawa,⁷ Iona Kondo ⁷, Man Cheung Alex Li,¹² Yutaka Matsubara,¹¹ Yasushi Muraki ¹¹, Shota Miyazaki ⁷, Greg Olmschenk ^{16,17}, Nicholas J. Rattenbury ¹², Yuki Satoh,⁷ Hikaru Shoji,⁷ Daisuke Suzuki ⁷, Yuzuru Tanaka,⁷ Paul J. Tristram,¹⁸ Tsubasa Yamawaki⁷ and Atsunori Yonehara ¹⁹

¹CNRS, UMR 7095, Institut d’Astrophysique de Paris, Sorbonne Université, 98 bis bd Arago, F-75014 Paris, France

²NASA Goddard Space Flight Center, Code 667, Greenbelt, MD 20771, USA

³Department of Astronomy, University of Maryland, College Park, MD 20742, USA

⁴Department of Astronomy, Graduate School of Science, The University of Tokyo, 7-3-1 Hongo, Bunkyo-ku, Tokyo 113-0033, Japan

⁵National Astronomical Observatory of Japan, 2-21-1 Osawa, Mitaka, Tokyo 181-8588, Japan

⁶Astronomical Observatory, University of Warsaw, Al. Ujazdowskie 4, PL-00-478 Warszawa, Poland

⁷Department of Earth and Space Science, Graduate School of Science, Osaka University, Toyonaka, Osaka 560-0043, Japan

⁸Institute of Natural and Mathematical Sciences, Massey University, Auckland 0745, New Zealand

⁹Laboratory for Particle Physics and Cosmology, Harvard University, Cambridge, MA 02138, USA

¹⁰Department of Applied Mathematics and Theoretical Physics, University of Cambridge, Wilberforce Road, Cambridge CB3 0WA, United Kingdom

¹¹Institute for Space-Earth Environmental Research, Nagoya University, Nagoya 464-8601, Japan

¹²Department of Physics, University of Auckland, Private Bag 92019, Auckland, New Zealand

¹³Department of Earth and Planetary Science, Graduate School of Science, The University of Tokyo, 7-3-1 Hongo, Bunkyo-ku, Tokyo 113-0033, Japan

¹⁴Instituto de Astrofísica de Canarias, Vía Láctea s/n, E-38205 La Laguna, Tenerife, Spain

¹⁵Department of Physics, The Catholic University of America, Washington, DC 20064, USA

¹⁶NASA Goddard Space Flight Center, Code 660, Greenbelt, MD 20771, USA

¹⁷Universities Space Research Association, Columbia, MD 21046, USA

¹⁸University of Canterbury Mt. John Observatory, PO Box 56, Lake Tekapo 8770, New Zealand

¹⁹Department of Physics, Faculty of Science, Kyoto Sangyo University, 603-8555 Kyoto, Japan

Accepted 2021 June 17. Received 2021 June 11; in original form 2021 March 12

ABSTRACT

Characterizing a planet detected by microlensing is hard if the planetary signal is weak or the lens-source relative trajectory is far from caustics. However, statistical analyses of planet demography must include those planets to accurately determine occurrence rates. As part of a systematic modelling effort in the context of a > 10-yr retrospective analysis of MOA’s survey observations to build an extended MOA statistical sample, we analyse the light curve of the planetary microlensing event MOA-2014-BLG-472. This event provides weak constraints on the physical parameters of the lens, as a result of a planetary anomaly occurring at low magnification in the light curve. We use a Bayesian analysis to estimate the properties of the planet, based on a refined Galactic model and the assumption that all Milky Way’s stars have an equal planet-hosting probability. We find that a lens consisting of a $1.9_{-1.2}^{+2.2} M_J$ giant planet orbiting a $0.31_{-0.19}^{+0.36} M_\odot$ host at a projected separation of 0.75 ± 0.24 au is consistent with the observations and is most likely, based on the Galactic priors. The lens most probably lies in the Galactic bulge, at $7.2_{-1.7}^{+0.6}$ kpc from Earth. The accurate measurement of the measured planet-to-host star mass ratio will be included in the next statistical analysis of cold planet demography detected by microlensing.

Key words: gravitational lensing: micro – planets and satellites: detection.

1 INTRODUCTION

During fall 2020, the hundredth exoplanet detection through gravitational microlensing was added to the NASA Exoplanet Archive

* E-mail: clement.ranc@protonmail.ch

database.¹ Although modest in amount when compared to the 4379 confirmed exoplanets to date and distributed in more than 3237 planetary systems (Schneider et al. 2011), this milestone enables an unprecedented look at the demography of cold exoplanets orbiting their host stars on wide orbits, with a typical semimajor axis of $\sim 0.5\text{--}10$ au. Microlensing detections dominate the population of confirmed planets below one Saturn mass and located beyond the ‘snow line’, i.e., the inner boundary of the protoplanetary disc where planet formation is most efficient, according to the core accretion theory (Lissauer 1987, 1993; Pollack et al. 1996). So, this sample represents a relatively new and unique opportunity for planet formation theories to compare predictions with observations, in a region of the parameter space largely unexplored by other planet detection techniques.

The first comparison of the microlensing planet occurrence rate with population synthesis models (Ida & Lin 2004; Mordasini 2018) identified a discrepancy between predictions of the core accretion theory’s runaway gas accretion process and observations (Suzuki et al. 2018). In particular, the observational results do not show any dearth of intermediate-mass giant planets, while the models predict 10 times fewer planets in the planet-to-host mass ratio range $10^{-4} < q < 4 \times 10^{-4}$. Resolving this discrepancy may have important implications in our understanding of the role played by the runaway gas accretion phase in the delivery of water to inner planetary orbits (Raymond & Izidoro 2017). The MOA collaboration is currently performing a systematic retrospective analysis including more than 10 yr of survey observations performed at the Mount John in New Zealand, to strengthen and expand the previous statistical results on microlensing planet occurrence rate (Gould et al. 2010; Sumi et al. 2010; Cassan et al. 2012; Shvartzvald et al. 2016; Suzuki et al. 2016; Udalski et al. 2018).

So far, this systematic analysis of previous survey data led to the discovery of several missed exoplanets (e.g., Kondo et al. 2019). The discovery presented in this article takes place in the context of this systematic modelling of past detections. We report the discovery of a new giant planet from the analysis of the microlensing event MOA-2014-BLG-472, initially detected by alert systems. The planetary signal for this event is not created by a caustic crossing. As a result, the planetary anomaly in the light curve has a low magnification, and the constraints on the physical parameters of the lens are weak. However, including planets like MOA-2014-BLG-472Lb in statistical studies on planet demography is crucial for the completeness of planetary occurrence rates.

This article describes the full analysis of MOA-2014-BLG-472. In Section 2, we recount the discovery of the event, describe the observations and select the data set used to model the event. In Section 3, we describe the full light-curve modelling process. In Section 4, we use a galactic model to derive the physical properties of the source and lens. Section 5 provides a summary of the analysis and concludes the article.

2 OBSERVATIONS AND DATA REDUCTION

The microlensing event MOA-2014-BLG-472 was discovered by the Microlensing Observations in Astrophysics (MOA, phase II; Sumi et al. 2003) collaboration and first alerted on 2014 August 16 at UT 11:40, i.e., $\text{HJD}' \approx 6885.99$.² The event is located at the J2000 equatorial coordinates (RA, Dec.) =

($18^{\text{h}} 00^{\text{m}} 19^{\text{s}}.40$, $-28^{\circ} 08' 56''.29$) in the MOA-II field ‘gb10.’ MOA observations were performed using a 1.8-m telescope (and its 2.2 deg^2 field of view camera, Sako et al. 2008) at the Mount John University Observatory in New Zealand with a cadence of 15 min in the custom wide-band MOA *R/I*-band filter, referred to as R_{MOA} . An anomaly was detected in real time by the MOA observers who issued an internal MOA alert on 2014 September 4. MOA’s implementation of the DIA method (Bond et al. 2001) has been used to extract the photometry of MOA observations.

The Optical Gravitational Lensing Experiment (OGLE, phase IV; Udalski, Szymański & Szymański 2015) was also monitoring this event and triggered an alert on the Early Warning System (EWS) website on 2014 August 26 at UT 11:06, naming the event OGLE-2014-BLG-1783. This event lies in the OGLE-IV field ‘BLG504.08,’ and has been observed with the 1.3-m-telescope located at Las Campanas Observatory in Chile (and its 1.4 deg^2 field-of-view camera), with a cadence of 1 h^{-1} . The anomaly has been detected by OGLE independently in their data, and an internal alert was sent on 2014 August 26 at UT 11:22. OGLE’s member Jan Skowron circulated among all the collaborations the first model performed, in real time, indicating a likely planet (with mass ratio of 0.0056) on 2014 September 20.

The final data sets consist of 13789 data points from MOA observations and used to model the microlensing light curve. We select five observing seasons (2 before and 2 after the event’s year) to prevent missing some potential variability in the baseline. The microlensing event has a weak maximal amplification of only 0.25 mag. However, due to the source star being a Red Clump giant ($I \sim 15.2$ mag), it is still well detectable/observable. Fig. 1 shows the magnification of the source flux as a function of time. The peak of magnification occurs at $\text{HJD}' \approx 6910$, and a clear anomaly starts at $\text{HJD}' \approx 6885$, first slowing down the magnification rise, then suddenly hiking up the magnification faster than a single-lens magnification pattern. Moreover, the anomaly occurs at an extremely low magnification, $A < 1.1$. The Fig. 1 displays 5-h bins for clarity purposes, but all the data are used during the modelling process.

As a consequence, the error bars are expected to play a major role in the final uncertainties on the physical parameters. Since the photometry pipelines typically underestimate the error bars, for each data set, we normalized the error bars on magnitudes, σ , so that the χ^2 per degree of freedom is $\chi^2/\text{d.o.f.} = 1$, and the cumulative sum of χ^2 is approximately linear. This procedure assumes a best-fitting model, and can be repeated as new plausible models are found. During the broad initial search in the parameter space, the error bars are not changed. Then, while exploring local χ^2 -minima, we use the normalization law (Yee et al. 2012)

$$\sigma'_i = k \sqrt{\sigma^2 + e_{\text{min}}^2}, \quad (1)$$

where σ' is the normalized error bar, the constant k is the rescaling factor, and the constant e_{min} mostly modifies the highly magnified data. For MOA-2014-BLG-472, we use $k = 1.205$ and $e_{\text{min}} = 2.763 \times 10^{-3}$.

3 LIGHT-CURVE MODELS

3.1 Single-lens model

We start modelling the event MOA-2014-BLG-472 by fitting the observations with a Paczyński light curve (Paczynski 1986), described by three independent parameters: the time (t_0) and projected separation (u_0) when lens and source are closest on the sky, and the

¹<https://exoplanetarchive.ipac.caltech.edu/>

² $\text{HJD}' = \text{HJD} - 2450000$.

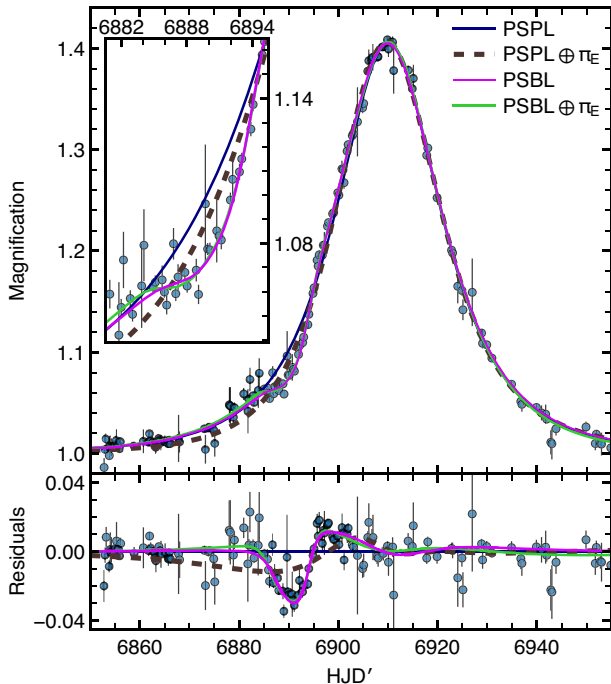


Figure 1. Magnification during the microlensing event MOA-2014-BLG-472 and the best point-source binary-lens model (PSBL; solid magenta line). For comparison, the black solid line, brown dashed line, and green solid line, respectively, show the rejected point-source point-lens (PSPL), PSPL including parallax, and PSBL with parallax models. MOA observations are displayed in blue. The inset shows a zoom in on the anomaly. In the lower panel, the residuals from the PSPL model are plotted in magnification units. For clarity, the plot uses 5-h bins to display the data (these bins are not used in the fit).

Einstein radius crossing time

$$t_E = \frac{\theta_E}{\mu_{\text{rel}}}, \quad (2)$$

where μ_{rel} is the lens-source relative proper motion in the geocentric reference frame and θ_E is the angular Einstein radius. These three parameters can be approximately estimated without any sophisticated numerical techniques. First, the peak of the event shown in Fig. 1 provides $\text{HJD}' \approx 6910$. Secondly, the peak-to-baseline flux ratio provides an estimate of the magnification at the peak of the event, $A_{\text{peak}} \approx 1.3$. Using Taylor series for the expression of the magnification yields $u_0 \approx 1$ at the peak. Thirdly, we derive the expected magnification at $t = t_0 + t_E$, and search for the corresponding flux in the light curve to find $t_E \approx 12$ d.

Above, we derived estimates for model parameters by assuming that the flux measurement comes entirely from the source star, which is almost never true. During the modelling process, the three parameters t_0 , u_0 , and t_E yield the magnification at any given date. To evaluate the goodness of fit of a model, two additional parameters are required to compute the observable: one describes the unlensed source flux f_{s,λ_i} , for any passband, λ_i ; the other is the excess flux, f_{b,λ_i} , resulting from the combination of any (and possibly several) ‘blend’ stars. The blend can be either the lens itself or an unrelated star or stars. At any time t , the total flux of the microlensing target is

$$\Phi_{\lambda_i}(t) = A(t)f_{s,\lambda_i} + f_{b,\lambda_i}, \quad (3)$$

where $A(t)$ is the source flux magnification at the date t , and λ_i is the MOA R passband.

Starting from the parameter estimated above, we use a Levenberg-Marquardt algorithm (Levenberg 1944) to find the best-fitting model parameters to be used as a starting position when searching for binary-lens models. We then use a Markov chain Monte Carlo (MCMC) algorithm to determine the uncertainties. At this stage, we remove the data during the anomaly, since a point-source point-lens model (hereafter ‘PSPL’) cannot (by definition) produce any anomaly. The median parameters and their credible intervals are: $t_0 = 6910.1 \pm 0.1$, $u_0 = 0.9 \pm 0.1$, and $t_E = 14 \pm 1$ d. For comparison with the other models presented in this article, the χ^2 value computed with the entire data set is $\chi^2 = 14744$. The best-fitting PSPL model is shown with a solid dark blue line in Fig. 1. In this figure, the data are binned for more clarity. We choose 5-h bins, such that for each bin, n , consisting of N_n data, the plotted uncertainty, σ_n'' , and magnification, A_n , are defined as

$$\sigma_n'' = \left(\sum_{j=1}^{N_n} \sigma_j'^2 \right)^{-1/2} \quad \text{and} \quad A_n = \sigma_n''^2 \sum_{j=1}^{N_n} \frac{A_j}{\sigma_j'^2}. \quad (4)$$

We do not use any binned data during the fitting process, though.

We introduce two additional parameters to assess whether the anomaly in the light curve may be explained by the non-inertial nature of the observer reference frame. These are the Northern and Eastern components of the microlens parallax vector in the geocentric frame, π_E , respectively $\pi_{E,N}$ and $\pi_{E,E}$, as defined in Gould (2004). The direction of vector π_E is the same as the instantaneous lens-source relative proper motion at $\text{HJD}' = 6910$, and its magnitude is the lens-source relative parallax in units of the angular Einstein ring radius, i.e.,

$$\pi_E = \frac{\pi_{\text{rel}}}{\theta_E}, \quad (5)$$

where $\pi_{\text{rel}} = 1 \text{ au}/D_L - 1 \text{ au}/D_S$, D_L is the distance to the lens and D_S the distance to the source. Starting from the best-fitting static model, we use an MCMC to find the best model with parallax, and estimate the uncertainties. We now include all the observations, since we search for a parallax signal that could explain the anomaly. Including the parallax in the model improves the χ^2 by $\Delta\chi^2 = -380$. The median and credible intervals of the parameters are: $t_0 = 6909.80 \pm 0.05$, $u_0 = 2.8 \pm 0.4$, $t_E = 6.2^{+0.8}_{-0.7}$ d, $\pi_{E,N} = 0 \pm 2$, and $\pi_{E,E} = 2.2 \pm 0.3$. The results from the MCMC show that the constraint on $\pi_{E,N}$ is very weak, allowing a broad range of acceptable values, including the solution $\pi_{E,N} = 0.0$ at a level $< 1\sigma$. The very large value of $\pi_E = 2.7^{+1}_{-0.5}$ results from the inability for the model to fit the anomaly. This can be seen in Fig. 1 that shows the best-fitting PSPL model with microlens parallax (hereafter ‘PSPL $\oplus\pi_E$ ’) with a thick brown dashed line. The static binary-lens model presented in Section 3.2 is preferred by $\Delta\chi^2 = -588$ and fits the anomaly.

3.2 Binary-lens models

In Section 3.1, we showed that the event MOA-2014-BLG-472 is not well described by a single-lens model, because the anomaly that occurs at $t \approx 6890$ cannot result from a parallax effect on a single lens. Hence, we search for plausible binary-lens, single-source models. Three additional parameters are required: the mass ratio of the secondary to primary lens component $q = M_2/M_1$, where M_2 (M_1) is the mass of the secondary lens (the mass of the primary lens, respectively); the separation in Einstein radius, s ; and the counterclockwise angle of the lens-source relative motion projected on to the sky plane with the lens binary axis (from the secondary to the

Table 1. Parameters for the best-fitting PSBL model and the corresponding statistical values from the posterior probability distribution function.

Parameter	Units	Best fit	MCMC results ^a
χ^2		13 776.36	...
$q/10^2$		0.568 450	$0.575^{+0.045}_{-0.042}$
s		0.475 423	0.47 ± 0.02
t_E	Days	14.787 693	14.6 ± 0.8
t_0	HJD'	6910.008 646	6910.01 ± 0.04
u_0		0.924 277	$0.94^{+0.08}_{-0.07}$
α	Deg	-145.685 730	-145.4 ± 0.9
$R_{\text{MOA},s}^b$		-11.846 185	-11.9 ± 0.2
$f_{b,R}/f_{s,R}^c$		0.454 891	0.4 ± 0.2
I_S		...	15.8 ± 0.2

^aMedian of the marginalized posterior distributions, with error bars displaying the 68.3 per cent credible interval around the median.

^bInstrumental source magnitude in MOA *R*-band filter.

^cRatio of MOA *R*-band instrumental blend and source flux. We do not convert the blend flux from the *R* to the *I* passband because the nature of the blend is unknown.

primary lens), α . For a binary lens model, we choose u_0 as the distance of closest approach between the lens centre of mass and the source.

We start exploring the parameter space searching for PSBL solutions using the best-fitting PSPL model parameters, and the initial condition grid search method introduced in Bennett (2010). In practice, for each set of $\{s, q\}$, we scan over $-\pi \leq \alpha \leq \pi$ with a 1.1° step. During this process, the best-fitting PSPL model parameters $\{t_0, u_0, t_E\}$ are kept fixed. We used 8 grid points in $\log \epsilon$, from -4.0 to -0.5 , with a 0.5 grid spacing, where $\epsilon = q/(1+q)$ is the planetary mass fraction. The separation values range from 0.1 to 10.0, evenly spaced on a grid of $\log s$, that includes:

- (i) 53 grid points for $\log \epsilon \leq -2.0$,
- (ii) 70 grid points for $\log \epsilon = -1.5$,
- (iii) 85 grid points for $-1.0 \leq \log \epsilon$.

For each model, we compute the χ^2 value and start 25 new fits from the best 25 models found on the grid. We only select one initial condition per $\{s, q\}$ couple, i.e., we use the best α value for a given set of $\{s, q\}$. At this stage, we release all the parameter constraints, and we use an adaptive version of the Metropolis algorithm optimizing the size of the proposal function during the exploration of the parameter space with a Monte Carlo method. The analysis of this set of fits leads us to identify four different models that meet our criterion $\Delta\chi^2 = \chi^2 - \chi^2_{\text{min}} \leq 500$, for further in-depth investigation. We use these models to define four classes of models in the next step, consisting in sampling the posterior distribution using several MCMC chains.

The two best-fitting models have the same caustic topology, with close values of s and q . One is the best-fitting model presented in Table 1. According to the second class of best models ($\Delta\chi^2 \approx 115$), the magnification peak would be due to one off-axis planetary caustic characterized by $s = 0.62798$ and $q = 8.8766 \times 10^{-3}$. However, this model does not fit the anomaly: ~ 80 per cent of the χ^2 difference compared to the best-fitting model comes from observations during the anomaly, and ~ 20 per cent comes from data between the anomaly and the event peak. This particular model is simply unable to reproduce the gradient of magnification during the anomaly, and must be rejected. The third class of models ($\Delta\chi^2 \approx 153$) involves a wide separation caustic. In this scenario, the main peak of the event is due to the central caustic, the source trajectory is passing in between the two components of the caustic, but this model does not properly fit the gradient of magnification during

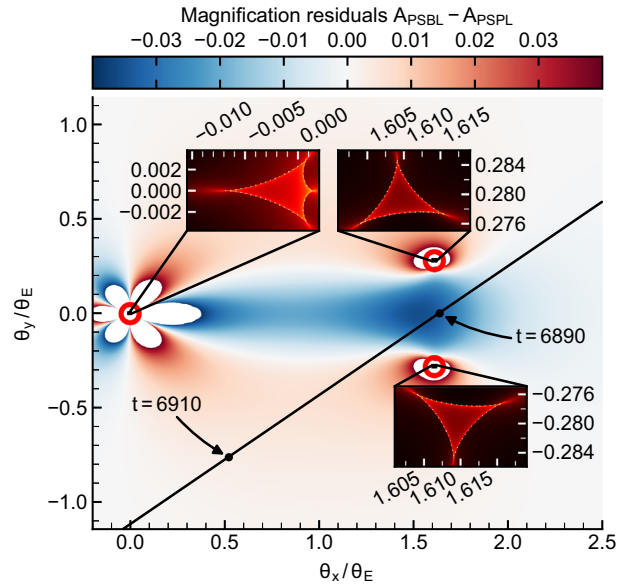


Figure 2. Caustic topology of the best-fitting PSBL model. The colour scale of the main plot refers to the magnification difference between the best PSBL and best PSPL models (except in the white regions around the caustic components, where the residuals are highest and not displayed). The caustic consists of three parts, located in the red circles. The insets display a zoom in on magnification maps in the vicinity of the caustic components in the source plane (dotted line). For convenience, we use two different logarithmic colour scales for the central and planetary caustics. The black line shows the source-lens trajectory, and the black dots the source position at HJD' = 6890 (anomaly peak) and HJD' = 6910 (event peak). Blue regions denote a de-magnification compared to a single lens.

the anomaly: ~ 69 per cent of the χ^2 increase compared to the best-fitting model occurs during the anomaly, and 24 per cent between the anomaly and the peak of the event. It is worth noting that the description of the tails of the event given by this model is also poorer. The fourth best model is substantially worse than the three others, does not fit the anomaly, nor the event peak, and is characterized by $\Delta\chi^2 \approx 423$ (98.6 per cent of this value comes from data in the interval HJD' = 6865-6910).

After checking the convergence of the MCMC chains, we use 50 000 samples to diagonalize the covariance matrix and optimize the posterior sampling. Fig. 2 displays the source trajectory relative to the caustics obtained with the best-fitting model. Table 1 shows the median of the marginalized posterior distributions. The error bars correspond to the 68.3 per cent credible interval around the median, derived from the 16 and 84 per cent percentile of the 1D marginalized posterior distribution. 1D cumulative functions and 2D covariances (and non-linearities) between the model parameters are shown in Fig. 3.

Table 1 and Fig. 3 only include the $u_0 > 0$ solution, but there is an exact degeneracy with a model characterized by $(u_0, \alpha) \mapsto -(u_0, \alpha)$, due to the symmetry of the lens. In practice, the other parameters remain unchanged, so the physical properties of source and lens are identical. Moreover, there is no close-wide ($s \mapsto 1/s$) discrete degeneracy, for the anomaly is due to the planetary caustic instead of the central caustic. In other words, the source apparent trajectory passes in the middle of minor image caustics, in a region where the magnification is lower than what would be observed if the lens were single. This feature is not easily reproducible with another lens geometry, which is, in part, the reason why there

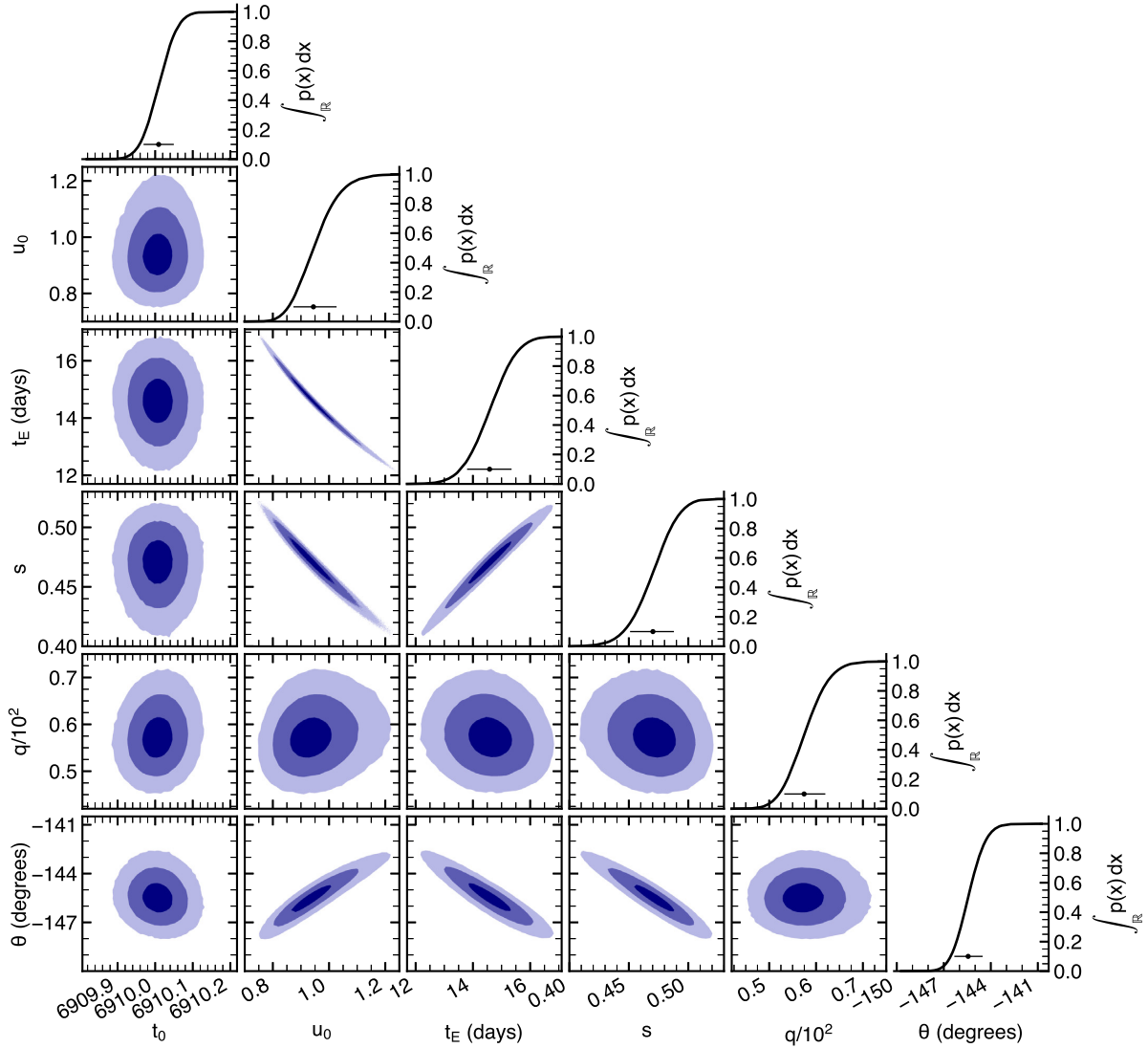


Figure 3. Correlation between the parameters for the PSBL model. The three shaded areas show the 1–3 σ credible regions, respectively, from the darkest to lightest colour. Plots in the diagonal display the marginal cumulative distribution of each parameter (solid line), the median of the distribution (dot), and the 68.3 per cent credible interval centered on the median. Plot prepared using the PYTHON package MOAnA (Ranc 2020).

are not many competing models for this event. Fig. 2 shows the magnification residuals between the PSBL and PSPL models, as well as magnification maps around the caustics computed with an adaptation of the library `luckylensing`³ (Liebig et al. 2015). The de-magnification regions appear in blue in this figure.

Although MOA-2014-BLG-472 is a low-magnification event, an anomaly is clearly identified at $t \approx 6890$. Due to the possibility that this anomaly is shaped by the effect of the physical size of the source, we introduce one more model parameter: the source radius crossing time, $t_* = \rho t_E = \theta_*/\mu_{\text{rel}}$, where ρ is the source angular radius in units of θ_E , i.e.,

$$\rho = \frac{\theta_*}{\theta_E}, \quad (6)$$

with θ_* the source angular radius. Hereafter, we refer to the resulting ‘finite-source binary-lens’ model as ‘FSBL.’ Finite source effects in microlensing light curves are usually sensitive to the stellar limb

darkening (Albrow et al. 1999), however, only if the source star crosses the caustic, which is not the case in MOA-2014-BLG-472.

We tried to extract constraints on t_* in two ways. One using an MCMC algorithm with no constraint on the parameters, and a large proposal step function. The other fixing t_* on a grid (25 nodes for $0.04 \text{ d} \leq t_* \leq 1.05 \text{ d}$), and searching for solutions with an MCMC algorithm. These two approaches do not provide any useful limit on t_* . In fact, the upper limit on t_* provided by the light curve is found between 1.0 and 1.5 d, corresponding to a χ^2 increase of respectively ~ 1 and ~ 7 . In Fig. 6, this upper limit falls at the edge between the 3 σ and 4 σ confidence regions of the posterior distribution, i.e., the final constraint on t_* exclusively comes from the galactic prior, rather than from the observations. This result is mainly due to the source trajectory relative to lens. As shown in Fig. 2, the PSBL solutions correspond to a caustic consisting in three very small parts of the source plane (a ‘central caustic’ and two ‘planetary caustics’). Along its trajectory, the source remains almost equidistant from the two planetary caustics, leaving the anomaly poorly magnified. However,

³Published at <https://github.com/smarnach/luckylensing>.

a detailed analysis unambiguously rules out the PSPL model by $\Delta\chi^2 = \chi_{\text{PSPL}}^2 - \chi_{\text{PSBL}}^2 = 968$.

Despite the relatively short time-scale of the event, we also considered PSBL models, including the microlens parallax (hereafter ‘PSBL $\oplus\pi_E$ ’). Although better by $\Delta\chi^2 \approx -12$, this model converges towards the unphysical large value $\pi_E = 2.5^{+0.9}_{-1.0}$ ($\pi_{E,N} = 2.4^{+0.9}_{-1.2}$ and $\pi_{E,E} = 0.3 \pm 0.1$), and leaves the other parameters almost unchanged (all the parameters are within 1σ of the static model). This means that a model with parallax does not change the interpretation of the lens. The best PSBL $\oplus\pi_E$ model is shown in green in Fig. 1. To assess whether the parallax detection is reliable, we compute the Bayesian information criterion (BIC) to take into account the effect of the additional free parameters in the models. The best PSBL model with parallax is now marginally preferred by $\Delta\text{BIC} \approx -0.03$. As a consequence, we cannot claim that the microlens parallax can be reliably measured using MOA observations of this event.

4 SOURCE AND LENS PHYSICAL PROPERTIES

4.1 Nature of the source star

As shown previously in Section 3, the source angular size is not detected in the light curve. Moreover, we do not have any colour information about the source. Despite a lack of observational information, this section shows that the nature of the source can be determined: it is most likely a red clump giant (RCG) star located in the Galactic bulge.

First, we build a colour–magnitude diagram (CMD) using the MOA-II R - and V -passband with stars within 2 arcmin around MOA-2014-BLG-472. Since the source brightness in R band found in Section 3 turns out to be the same as RCG stars, we assume that the source belongs to the RCG. Doing so, we implicitly reject the scenario with a foreground main-sequence source. Although not impossible, this scenario is unlikely because the probability for a star to be lensed is proportional to D_S^2 (Paczynski 1996). Also, the foreground is much less populated by main-sequence stars at a magnitude $I \approx 16$, than the background.

The second step is to calibrate the instrumental MOA-II R_{MOA} magnitude by cross-referencing stars from the MOA-II DOPHOT catalogue with stars in the OGLE-III catalogue. We use these stars to build a catalogue with magnitudes in the standard Kron–Cousins I and Johnson V passbands (Szymański et al. 2011). In OGLE-III catalogue, we identify 7446 stars located less than 2 arcmin from MOA-2014-BLG-472, while we find 1222 stars in the MOA-II catalogue. Fig. 4 shows the resulting OGLE-III ($V - I$, I) CMD. Following the method described in Nataf et al. (2016), we identify RCG stars to derive their centroid (red circle in Fig. 4). A total of 818 stars are cross-matched, including 251 RCG stars (see Fig. 4). Since we assume a source that belongs to the RCG, we select those stars to derive an empirical linear law between OGLE-III I and MOA-II R_{MOA} magnitudes. Fig. 5 displays the aforementioned cross-matched stars, the RCG stars used in the linear fit, and outliers. The outliers are identified by following the methodology described in section 3 of Hogg, Bovy & Lang (2010), taking alternatively into account the error bars of I and R_{MOA} . We remove from the final fit the RCG stars that are classified as outliers in both cases. During this process, we note that an underestimate of the photometric error bars seem to be responsible for being classified as an outlier. The final linear fit is then performed following section 7 of Hogg et al. (2010), taking into account 2D uncertainties. The resulting empirical law reads, $I = a_0 + a_1 R_{\text{MOA}}$, with $a_0 = 27.58 \pm 0.06$ and $a_1 = 0.992 \pm 0.005$. These values correspond to the median of the marginalized posterior

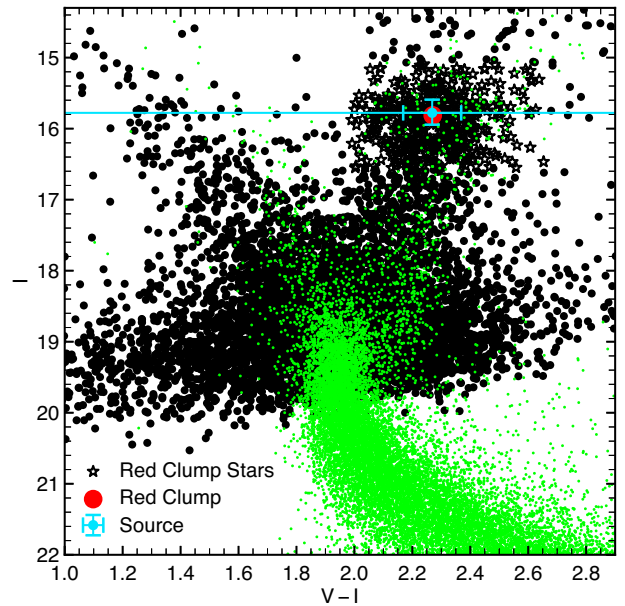


Figure 4. The black dots show a CMD in the standard Kron–Cousins I and Johnson V photometric systems of OGLE-III stars selected within 2 arcmin around the target. The RCG centroid is indicated by the red circle, and the RC stars are shown as black stars. The source brightness and the estimated source colour are shown by the cyan point. The colour dispersion of the RC stars mostly accounts for the source colour error. The cyan horizontal line reminds us that we only measured the source brightness, and the source colour fully follows from the assumption that the source belongs to the RC. The green dots show the *Hubble Space Telescope* CMD from Holtzman et al. (1998) shifted to the bulge distance and extinction derived for the MOA-2014-BLG-472 line of sight.

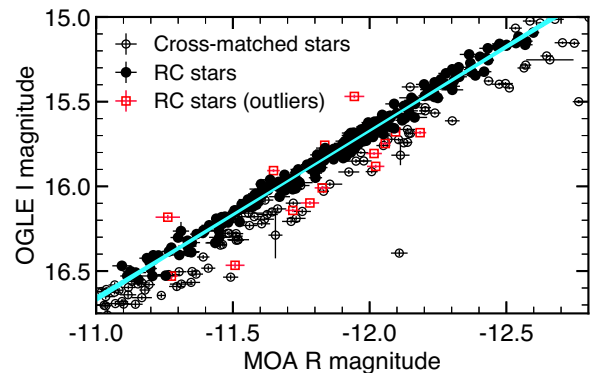


Figure 5. Empirical law between OGLE I magnitude and the instrumental R_{MOA} magnitude of stars located at an angular separation less than 2 arcmin from MOA-2014-BLG-472. RCG stars (black dots) only are used in the linear fit (except the outliers displayed as red squares). Black circles correspond to stars that do not belong to the RCG (most of them are foreground main-sequence stars). The cyan region is an envelop holding 100 000 randomly chosen samples.

distributions (i.e., the two values do not necessarily represent a good fit), sampled with an MCMC algorithm. The error bars display the 68.3 per cent credible interval around the median, derived from the 16 and 84 per cent percentile of the corresponding marginalized posterior distribution. Fig. 5 shows the envelop that holds 100 000 randomly chosen samples.

The third step is to use the calibration law found in step 2 to derive the I -band source magnitude. Fig. 4 shows the source location in the OGLE CMD (cyan point), when its colour is assumed to be the same as the CMD centroid at the corresponding brightness ± 0.4 mag, and with the same dispersion. In practice, for each value of the source brightness derived from the previous step, the source colour is described by a Gaussian distribution, which mean coincides with the centroid of RCG stars, and with a standard deviation derived from the colour dispersion of RCG stars that have the same brightness as the source ± 0.4 mag. Under this assumption, the following paragraphs explain how we estimate the source radius from its brightness and colour.

To do so, we measure the extinction and reddening of stars within 2 arcmin around MOA-2014-BLG-472. The centroid of the RCG stars is $(V - I)_{\text{RCG}} = 2.27 \pm 0.02$ and $I_{\text{RCG}} = 15.8 \pm 0.1$. The absolute magnitude of a source located in the Galactic bulge is $M_{I,\text{RCG}} = -0.17 \pm 0.05$ (Chatzopoulos et al. 2015; Nataf et al. 2016) and its intrinsic colour is $(V - I)_{\text{RCG},0} = 1.06$ (Bensby et al. 2013). We use a new Galactic model (Koshimoto & Ranc 2021; Koshimoto, Baba & Bennett 2021) to estimate the distance modulus of the source, $\mu = 14.60^{+0.21}_{-0.15}$, corresponding to $D_S = 8.34^{+0.86}_{-0.57}$ kpc. As expected, these values are consistent with the assumption we made of an RCG source. The new Galactic model improves several aspects of previous ones (Bennett et al. 2014; Zhu et al. 2017), for instance by taking into account the change in the velocity dispersion within the disc, with respect to the distance to the Galactic Centre. Since the extinction and reddening mostly occurs during the first kiloparsecs away from Earth, the dereddened source magnitude is $I_{s,0} = I_s + M_{I,\text{RCG}} + \mu - I_{\text{RCG}}$, i.e., $I_{s,0} = 14.4 \pm 0.3$, and $(V - I)_{s,0} = 1.06 \pm 0.14$. The corresponding extinction $A_I = 1.39^{+0.16}_{-0.22}$, and colour excess $E(V - I) = 1.2 \pm 0.1$ found are in good agreement with the $A_I = 1.47$ and $E(V - I) = 1.21$ derived from Gonzalez et al. (2012).

Finally, the angular source size can be estimated using the empirical relation (Boyajian, van Belle & von Braun 2014)

$$\log\left(\frac{2\theta_*}{\text{mas}}\right) = 0.501414 - 0.2I_{s,0} + 0.419685(V - I)_{s,0}, \quad (7)$$

inferred from stars with colors corresponding to $3900 \text{ K} < T_{\text{eff}} < 7000 \text{ K}$ (Bennett et al. 2017). In equation (7), ‘mas’ denotes milliarcsec. The resulting source angular radius yields the source radius, $R_* = \theta_* D_S$, and the source radius crossing time, $t_* = \theta_* / \mu_{\text{rel}}$, shown in Fig. 6. With $\theta_* = 5.8^{+1.2}_{-1.0} \mu\text{as}$ (‘ μas ’ denotes micro-arcsec) and $R_* = 10.5^{+1.8}_{-1.5} R_\odot$, we check that the source is a red giant star of the Galactic bulge, as we assumed.

The exact origin of the blend flux remains unknown. The ratio of the blend flux to the source flux for the binary-lens models, $f_{b,R}/f_{s,R}$, is 0.4 ± 0.2 (see Table 1). It may be due to one or several stars, including the lens, blended into the point spread function. As a consequence, the blend flux cannot be used to characterize further the nature of the lens.

4.2 Nature of the lens

The main difficulty of the lens characterization is that the light-curve modelling returns only one parameter that is sensitive to the mass and distance, namely, the Einstein time-scale defined in equation (2). The mass-distance dependence of t_E appears in the expression of the angular Einstein radius; i.e.

$$\theta_E = \sqrt{\frac{4GM}{c^2 D_S} \left(\frac{D_S}{D_L} - 1\right)}, \quad (8)$$

where M is the lens mass, D_S and D_L are the distances to the source and lens, c is the speed of light, and G is the gravitational constant.

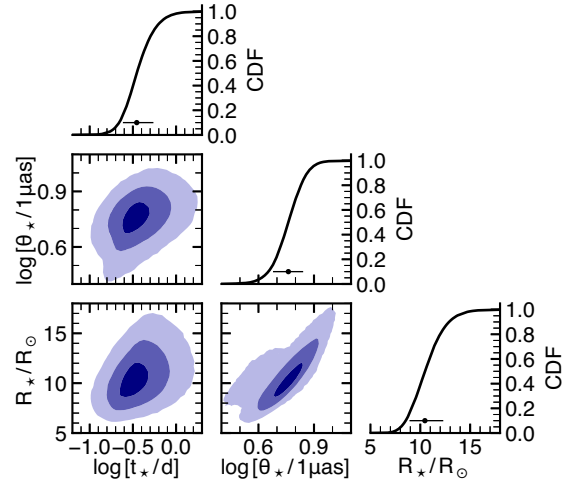


Figure 6. Correlation between the parameters for the best-fitting model. The three shaded areas show the 1–3 σ confidence regions, respectively, from the darkest to lightest colour. Plots in the diagonal displays the marginal cumulative distribution function of each parameter (solid line), the median of the distribution (dot), and the 68.3 per cent credible interval centred on the median. Plot prepared using the python package MOAnA (Ranc 2020).

We use a galactic model of the Milky Way to predict the distribution of angular Einstein radii, source distances and lens-source relative parallaxes as introduced in equation (5)

$$\pi_{\text{rel}} = \frac{1 \text{ au}}{D_L} - \frac{1 \text{ au}}{D_S}, \quad (9)$$

from the event coordinates. This model assumes that all stars have an equal planet hosting probability. Then, we use these predictions as priors to derive the total mass of the lens using equations (8) and (9), i.e.,

$$M = 0.1228 M_\odot \left(\frac{\theta_E}{1 \text{ mas}}\right)^2 \left(\frac{\pi_{\text{rel}}}{1 \text{ mas}}\right)^{-1}, \quad (10)$$

and the distance to the lens,

$$D_L = 1 \text{ kpc} \left(\frac{\pi_{\text{rel}}}{1 \text{ mas}} + \left(\frac{D_S}{1 \text{ kpc}}\right)^{-1}\right)^{-1}. \quad (11)$$

Since the angular Einstein radius measurements via microlensing is typically > 1 per cent, the precision of the lens mass estimation is expected to be > 2 per cent; we choose the significant digits of the constant in equation (10) accordingly. Finally, the host-star and planet masses can be found from the measurement of the mass ratio in Section 3.2, i.e.,

$$M_1 = \frac{M}{1+q} \quad \text{and} \quad M_2 = \frac{qM}{1+q}. \quad (12)$$

The results of the Bayesian analysis are summarized in Table 2.

The lens likely consists of a $1.9^{+2.2}_{-1.2} M_J$ Jupiter-mass planet orbiting a $0.31^{+0.36}_{-0.19} M_\odot$ M-dwarf star. As expected, the lack of source size measurement is responsible for large uncertainties on the mass of each component of the lens system. The planet-host star projected separation is 0.75 ± 0.24 au. If we assume a circular orbit, this value translates into a mean semimajor axis 0.96 ± 0.31 au. This planetary system lies at a distance $7.2^{+0.6}_{-1.7}$ kpc.

In Fig. 7, the light grey shading indicates the thin and thick-disc contribution to the posterior distribution (black solid curve), while the dark grey shading indicated the spheroid and bulge contribution to

Table 2. Lens and source properties derived from the Bayesian analysis of Section 4.

Parameter	MCMC results ^a	Units
Host mass M_1	$0.31^{+0.36}_{-0.19}$	M_\odot
Planet mass M_2	$1.9^{+2.2}_{-1.2}$	M_J
Projected separation a_\perp	0.75 ± 0.24	au
Deprojected separation a	0.96 ± 0.31	au
Lens distance D_L	$7.2^{+0.6}_{-1.7}$	kpc
Einstein radius ^b θ_E	$0.24^{+0.09}_{-0.08}$	mas
Lens-source proper motion ^b $\mu_{\text{rel,G}}$	$6.0^{+2.3}_{-2.0}$	mas yr^{-1}
Source magnitude $I_{S,0}$	14.4 ± 0.3	mag
Source colour $(V - I)_{S,0}$	1.06 ± 0.14	mag
Extinction A_I	$1.39^{+0.16}_{-0.22}$	mag
Reddening $E(V - I)$	1.2 ± 0.1	mag
Source angular radius θ_*	$5.7^{+1.2}_{-1.0}$	μas

^aMedian of the marginalized posterior distributions, with error bars displaying the 68 per cent credible interval around the median.

^bGalactic prior.

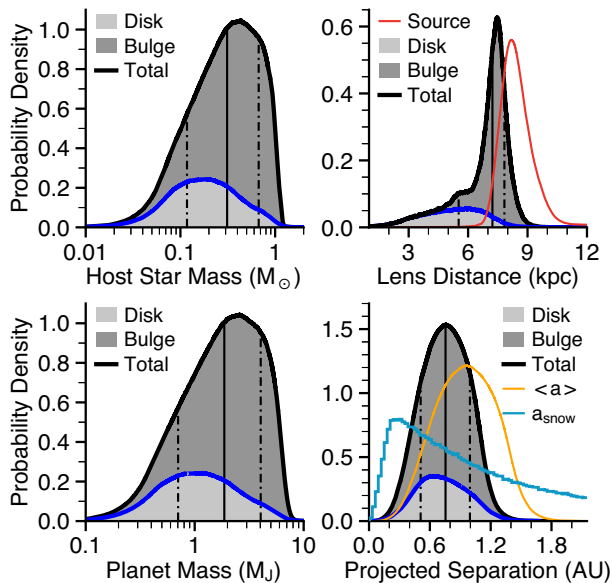


Figure 7. 1D marginalized posterior probability density function of the host star mass (upper left panel), distance to the lens (upper right panel), planet mass (lower left panel), and projected separation (lower right panel). Two shaded areas are separated by a dark blue line. They show the contribution of the thin and thick discs (light grey), and the spheroid and bulge (dark grey) to the posterior distribution (black line). The upper right panel also displays the prior distribution on the source distance (red dashed line), derived from the galactic model. The lower right panel includes the probability density function of the deprojected separation (orange line), $\langle a \rangle$, and snow line position (light blue line), a_{snow} .

the posterior distribution. Although these profiles raise the possibility of a lens lying in the disc, they suggest that a bulge lens is much more likely.

5 SUMMARY AND DISCUSSION

We have reported the discovery of a new Jupiter-mass planet, MOA-2014-BLG-472Lb, discovered through a low magnification anomaly during the microlensing event MOA-2014-BLG-472. The anomaly was due to the source star passing in between the two off-axis

components of a close caustic, consistent with a planet-to-host-star mass ratio $q = 5.75^{+0.45}_{-0.42} \times 10^{-3}$. Since microlensing in the Milky Way is most often caused by M-dwarfs lenses, this mass ratio corresponds typically to the domain of giant planets. The projected separation between the planet and the host star is $s = 0.47 \pm 0.02$ Einstein radius. The $s \leftrightarrow 1/s$ degeneracy does not exist for this event, because the anomaly is not due to the central caustic. An exact geometrical degeneracy exists, leaving the lens physical parameters unchanged, though.

Due to its low magnification (maximum $A \approx 1.4$), and anomaly occurring at an extremely low magnification ($A \approx 1.06$), we did not detect features resulting from the angular size of the source. Without this measurement, we cannot use the light curve to measure θ_E . However, we used a Galactic model to predict the distribution of the Einstein radius, source distance, relative lens-source proper motion, and microlens parallax. The resulting constraints on the lens physical properties are weak, but a low-mass ratio in conjunction with a likely low-mass host enables us to put the mass of the companion in the planetary mass regime.

Including planets like MOA-2014-BLG-472Lb in statistical studies on planet demography is crucial for the completeness of planetary occurrence rates. The event MOA-2014-BLG-472 (including the anomaly) was intensively monitored by the MOA survey. Interestingly, although the physical parameters of MOA-2014-BLG-472Lb are not tightly constrained, the mass ratio, q , and the projected separation, s , are both precisely measured, and not degenerate. Events without close-wide degeneracy are not so common in statistical analyses. Since MOA-2014-BLG-472 does not suffer from it, it is an important add on to the new MOA sample of microlensing planets, that will be used in the next statistical analysis.

ACKNOWLEDGEMENTS

The authors thank the anonymous referee, whose comments and suggestions improved the manuscript. CR thanks Anne Shrestha for stimulating discussions. This work was carried out within the framework of the ANR project COLD-WORLDS supported by the *Agence Nationale de la Recherche* (French National Agency for Research) with the reference ANR-18-CE31-0002. The work of CR, DPB, NK, YH, and AB was supported by NASA under award number 80GSFC17M0002. JS acknowledges support from the National Science Center, Poland grant MAESTRO 2014/14/A/ST9/00121. The MOA project is supported by JSPS KAKENHI grant No. 19KK0082 and 20H04754. This research has made use of the NASA Exoplanet Archive, which is operated by the California Institute of Technology, under contract with the National Aeronautics and Space Administration under the Exoplanet Exploration Program.

DATA AVAILABILITY

The original data underlying this article can be accessed from the NASA Exoplanet Archive MOA Resources, <https://exoplanetarchive.ipac.caltech.edu/docs/MOAMission.html>. The derived data generated in this research will be shared on reasonable request to the corresponding author until they are added to the NASA Exoplanet Archive, at https://exoplanetarchive.ipac.caltech.edu/docs/contributed_data.html.

REFERENCES

- Albrow M. D. et al., 1999, *ApJ*, 522, 1011
 Bennett D. P., 2010, *ApJ*, 716, 1408

- Bennett D. P. et al., 2014, *ApJ*, 785, 155
 Bennett D. P. et al., 2017, *AJ*, 154, 68
 Bensby T. et al., 2013, *A&A*, 549, A147
 Bond I. A. et al., 2001, *MNRAS*, 327, 868
 Boyajian T. S., van Belle G., von Braun K., 2014, *AJ*, 147, 47
 Cassan A. et al., 2012, *Nature*, 481, 167
 Chatzopoulos S., Fritz T. K., Gerhard O., Gillessen S., Wegg C., Genzel R., Pfuhl O., 2015, *MNRAS*, 447, 948
 Gonzalez O. A., Rejkuba M., Zoccali M., Valenti E., Minniti D., Schultheis M., Tobar R., Chen B., 2012, *A&A*, 543, A13
 Gould A., 2004, *ApJ*, 606, 319
 Gould A. et al., 2010, *ApJ*, 720, 1073
 Hogg D. W., Bovy J., Lang D., 2010, preprint([arXiv:1008.4686](https://arxiv.org/abs/1008.4686))
 Holtzman J. A., Watson A. M., Baum W. A., Grillmair C. J., Groth E. J., Light R. M., Lynds R., O’Neil E. J., Jr., 1998, *AJ*, 115, 1946
 Ida S., Lin D. N. C., 2004, *ApJ*, 604, 388
 Kondo I. et al., 2019, *AJ*, 158, 224
 Koshimoto N., Ranc C., 2021, *A Tool for Gravitational Microlensing Events Simulation*
 Koshimoto N., Baba J., Bennett D. P., 2021, preprint([arXiv:2104.03306](https://arxiv.org/abs/2104.03306))
 Levenberg K., 1944, *Q. Appl. Math.*, 2, 164
 Liebig C., D’Ago G., Bozza V., Dominik M., 2015, *MNRAS*, 450, 1565
 Lissauer J. J., 1987, *Icarus*, 69, 249
 Lissauer J. J., 1993, *ARA&A*, 31, 129
 Mordasini C., 2018, *Planetary Population Synthesis*. Springer International Publishing, Cham, p. 2425
 Nataf D. M. et al., 2016, *MNRAS*, 456, 2692
 Paczyński B., 1986, *ApJ*, 304, 1
 Paczynski B., 1996, *ARA&A*, 34, 419
 Pollack J. B., Hubickyj O., Bodenheimer P., Lissauer J. J., Podolak M., Greenzweig Y., 1996, *Icarus*, 124, 62
 Ranc C., 2020, *Microlensing Observations ANALYSIS tools*
 Raymond S. N., Izidoro A., 2017, *Icarus*, 297, 134
 Sako T. et al., 2008, *Exp. Astron.*, 22, 51
 Schneider J., Dedieu C., Le Sidaner P., Savalle R., Zolotukhin I., 2011, *A&A*, 532, A79
 Shvartzvald Y. et al., 2016, *MNRAS*, 457, 4089
 Sumi T. et al., 2003, *ApJ*, 591, 204
 Sumi T. et al., 2010, *ApJ*, 710, 1641
 Suzuki D. et al., 2016, *ApJ*, 833, 145
 Suzuki D. et al., 2018, *ApJ*, 869, L34
 Szymański M. K., Udalski A., Soszyński I., Kubiak M., Pietrzyński G., Poleski R., Wyrzykowski Ł., Ulaczyk K., 2011, *Acta Astron.*, 61, 83
 Udalski A., Szymański M. K., Szymański G., 2015, *Acta Astron.*, 65, 1
 Udalski A. et al., 2018, *Acta Astron.*, 68, 1
 Yee J. C. et al., 2012, *ApJ*, 755, 102
 Zhu W. et al., 2017, *AJ*, 154, 210

This paper has been typeset from a $\text{\TeX}/\text{\LaTeX}$ file prepared by the author.